JOURNAL OF CATALYSIS **165,** 22–32 (1997)
ARTICLE NO. CA971462

Characterization of Catalysts Based on Titanium Silicalite, TS-1, by Physicochemical Techniques

E. Duprey,* P. Beaunier,† M.-A. Springuel-Huet,* F. Bozon-Verduraz,‡ J. Fraissard,* J.-M. Manoli,† and J.-M. Brégeault*,[1]

*Département de Chimie, URA 1428 du CNRS, Catalyse Homogène et Chimie des Surfaces, Tour 54-55, Case 196, Université Pierre et Marie Curie, 4 place Jussieu, F-75252 Paris Cedex 05, France; †URA 1106 du CNRS, Réactivité de Surface, Tour 54-55, Case 178, Université Pierre et Marie Curie, F-75252 Paris Cedex 05, France; and ‡Chimie des Matériaux Divisés et Catalyse, Tour 44-45, Case 7090, Université Denis Diderot, 2 place Jussieu, F-75251 Paris Cedex 05, France

Received March 15, 1996; revised July 27, 1996; accepted September 3, 1996

Two titanium silicalite-1 samples (A and B) with similar particle sizes have been characterized by powder X-ray diffraction, FT-IR and FT-Raman spectroscopy, UV–visible diffuse reflectance spectroscopy (DRS), transmission electron microscopy with X-ray energy dispersion spectrometry (to analyze grains and ultramicrotomed sections), and xenon-129 NMR. Activity and selectivity for the epoxidation of oct-1-ene by phosphate-free 30% aqueous hydrogen peroxide have been investigated. The critical factors governing the activities of the samples with molar ratios Si : Ti $\approx$ 39 (sample A) and 32 (sample B) are the distribution of titanium within the microporous materials and within the extraframework titania (crystalline anatase or amorphous phase as evidenced by UV–visible DRS, FT-Raman spectroscopy, and electron microscopy). Xenon-129 NMR chemical shifts, $\delta_{exp} = f(n)$ (n = number of adsorbed xenon atoms per gram of anhydrous sample), depend dramatically on extraframework impurities and Ti(IV) dispersion. Pure silicalite and nearly perfect TS-1 (sample A) are not differentiated by xenon-129 NMR, a fact which is tentatively attributed to the "atomic dispersion" of the titanium in sample A, as evidenced by X-ray EDS and by the channel dimensions.

INTRODUCTION

As part of a comprehensive research program on oxidation reactions, we have studied the catalytic epoxidation of alkenes by hydrogen peroxide in the presence of tungsten peroxo-complexes (1–3). It is intended to compare the behavior of these catalysts with that of transition-metal-containing molecular sieves (TMCMS). In this paper, attention is focused on the characterization of titanium silicalite-1 catalysts (TS-1).

Among the TMCMS, titanium silicalites have been studied intensively in the past decade (4, 5). Titanium silicalite-1, which has an MFI structure, is a remarkable microporous catalyst for selective oxidation by aqueous hydrogen peroxide under mild conditions (6).

From environmental considerations and for fine chemical production, 30% aqueous hydrogen peroxide is the oxidant of choice; it does not pose the handling problems associated with concentrated peroxides (7, 8), and the by-product is water. Because of simpler workup (ease of separation, regeneration, and handling) and reduced environmental problems compared to homogeneous (9, 10) or phase transfer catalysis systems (10, 11), heterogeneous processes involving TS-1 have been developed by Enichem (6). TS-1 is now used for the production of two industrial chemicals: catechol and hydroquinone have been produced since 1986 by the hydroxylation of phenol with H_2O_2 (12), a process which competes with the homogeneous systems developed earlier by Rhône–Poulenc (13, 14). In the conversion of cyclohexanone into cyclohexanone oxime in the presence of ammonia, H_2O_2 and TS-1 offer a substantial reduction in coproduct formation (15, 16). TS-1 is also a particularly active catalyst for the epoxidation of low-molecular-weight linear alkenes (6, 12). Hence, TS-1 and related materials appear very suitable for developing clean homolytic or heterolytic processes.

There is considerable question and/or dispute as to the exact nature of the active sites, although several physicochemical methods have been used to probe titanium environments in titanium silicalite (17–32); many samples seem to contain framework Ti(IV) with extraframework Ti(IV) and/or impurities (Na^+, K^+, etc). It has been postulated that the unique catalytic properties of titanium silicalite in oxidation reactions involving hydrogen peroxide are related to tetrahedral framework titanium (6, 17) with every Ti(IV) surrounded by $-O-Si-O-Si-O-$ in all directions. Thus, the titanium centers are isolated from each other by $[SiO_4]_n$ sequences. It has been proposed that the molar ratio of Si to Ti cannot be less than 24 (17). However, more recently it was claimed that titanium-rich silicalite having a molar ratio in

[1] To whom correspondence should be addressed.

0021-9517/97 $25.00

the lattice framework of 8 to 23 also converts alkenes to epoxides very effectively (33, 34). Synthetic procedures use the fact that tetravalent alkoxo-, oxo-, or peroxo- moieties have a marked tendency to oligomerize in the stage of gel preparation, which is followed by crystallization under autogeneous pressure. This makes the synthesis of pure TS-1 and of other TMCMS rather difficult to control, and several recipes have been proposed (4, 35, 36). As already mentioned, several groups have worked on TS-1 synthesis, and their results differ significantly (4, 6). The catalytic performances of a standard titanium molecular sieve, EUROTS-1, were recently evaluated in four European universities (37).

Usually there are large differences in activity between different TS-1 specimens or, more generally, TMCMS samples. It is sometimes difficult to differentiate between active and less active samples using conventional analytical techniques; smaller particles were found to be more active than larger particles (38). To improve the catalytic reactions, it is necessary to examine analytical results carefully in order to select active TS-1 samples or related molecular sieves.

In the present study we used a catalytic test (epoxidation of oct-1-ene), X-ray diffraction (XRD), Fourier transform infrared spectrometry (FTIR), Raman spectroscopy, UV–visible diffuse reflectance spectroscopy (UV–visible DRS), transmission electron microscopy (TEM), and X-ray energy dispersion spectrometry (X-ray EDS). For the first time, special emphasis is centered on the combination of ^{129}Xe NMR spectroscopy and X-ray EDS, in order to obtain further correlations of properties of microporous materials with Si to Ti ratios higher than 30 and their structure.

EXPERIMENTAL

Materials

Both samples were synthesized according to procedures given in the patent literature (39). In sample A (wt% Ti $\approx$ 1.9, wt% Si $\approx$ 42.4) the Ti(IV) was almost completely in the framework (*vide infra*); the extraframework fraction cannot be estimated. Sample B is a mixture of phases containing mainly TS-1 (wt% Ti $\approx$ 2.4, wt% Si $\approx$ 44.7). The calcination conditions were heating rate, 5°C/min under flowing dioxygen (100 to 300 ml/min), and maximum temperature, 555°C (5 h). After equilibration at room temperature, thermogravimetric analysis of samples A and B showed that they lost *ca.* 3.5% of water. The above results indicate that the titanium silicalites have the general formula $x\mathrm{TiO_2}\cdot(1-x)\mathrm{SiO_2}$, with x about 0.025 and 0.030_5 for A and B, respectively.

Acetone (Prolabo RP), oct-1-ene (Aldrich, Fluka >97%), GLC internal standards (methyl *tert*-butyl ether, etc.), and authentic samples of major products were used as received. Aqueous solutions of hydrogen peroxide (30%) were purchased from Prolabo or Aldrich (phosphate-free or with less than 2 ppm of phosphate stabilizers). The active oxygen contents of H_2O_2 solutions were analyzed by iodometric titration. Pure silicalite and KY zeolite, obtained from UOP, were used as references in the ^{129}Xe NMR experiments.

Catalytic Tests

The epoxidation of oct-1-ene was carried out to evaluate the catalytic properties of the two selected samples. A 65-ml round-bottomed Schlenk flask was charged with 50 mg of catalyst, 4.5 ml of acetone, 10.2 mmol of oct-1-ene, and 3.4 mmol of H_2O_2 as a 30% aqueous solution. The Schlenk flask was then placed under reflux in an oil bath thermostated at 60°C and stirred magnetically for 2 h. After the reaction, the mixture was transferred to a vial and centrifuged to separate the solid catalyst from the solution. Products were analyzed with an internal standard on a Delsi 30 gas chromatograph equipped with a 0.25 mm $\times$ 50 m OV 1701 capillary column and a flame ionization detector linked to a Delsi Enica 10 integrator. GC/MS data were obtained at 70 eV on a mass spectrometer (Delsi–Nermag) coupled with a GC apparatus.

Characterization of Catalysts by Physicochemical Techniques

Chemical analyses were carried out at the Service Central d'Analyse (CNRS-Lyon) by inductive coupling plasma-atomic emission spectroscopy (ICP-AES) after alkaline fusion with $Li_2B_4O_7$.

XRD patterns (Cu$K\alpha$ radiation) were recorded on a Siemens D500 automatic diffractometer with 2θ from 5° to 55° and scanning rate of 0.6°(2θ) min^{-1} [0.02° (2θ) step and 2.0 s counting time]. The diffractometer was calibrated to within 0.02° (2θ) using a standard SiO_2 sample. The elementary crystalline cell parameters were determined on the basis of selected reflections in the 10–40° range for 2θ.

FTIR spectra were obtained in the transmission mode with a Bruker IFS45 spectrometer. Standard potassium bromide disks (8 tons cm^{-2}) with very dilute mixtures of catalyst and dry KBr were used. Water is known to influence the intensity of the 960 cm^{-1} peak (18, 20, 27); for comparison, samples with approximatively the same water content were studied. Control experiments with Nujol suspensions between two cesium bromide plates gave comparable but less well-defined spectra.

Raman spectra were recorded on a Jobin–Yvon U_{1000} spectrometer with a resolution of 4 cm^{-1}. The 647-nm excitation line of a krypton laser was used at 80–100 mW. The powder samples were mounted on a disk rotating at about 1000 rpm to avoid decomposition and/or photoreduction by the laser beam. A reference (wt% $K_2SO_4 \approx 4$) was incorporated into the sample to compare the responses. For small samples which fluoresce under visible illumination, Fourier transform Raman spectrometers give improved results. Spectra with a better signal-to-noise ratio were

obtained with a Bruker RFS 100S spectrometer using a Nd–YAG laser, operating at 1064 nm with power output *ca.* 150–300 mW and resolution 2–4 cm^{-1}. They are selected for presentation in the paper.

UV–visible diffuse reflectance spectrometry was performed on a Beckman 5270 spectrophotometer equipped with an integration sphere and coupled with a HP microcomputer. Calcined samples equilibrated with water vapor at room temperature were studied. Outgassing treatments on a vacuum line were not used in our analysis since they have been considered by several authors (20); the catalysts were tested in the presence of air.

Transmission electron microscopy and X-ray energy dispersion spectrometry were performed using a LINK AN 10000 system (Si–Li diode detector) connected to a JEOL JEM 100CXII transmission electron microscope operating at 100 kV and equipped with an ASID 4D scanning device (STEM mode). Samples were examined either as crystallites dispersed on copper grids or as ultramicrotomed sections using conventional sample preparation and imaging techniques (40). The X-rays emitted from the specimen upon electron impact were collected in the 0–20 keV range for 200–400 s. The X-ray EDS analyses were obtained either from large domains (e.g., 100×130 nm^2 to 600×800 nm^2) or from smaller domains (spot beam analyses: 175 or 1250 nm^2). Atomic compositions (%) were obtained with the 2 LINK program (RTS-2/FLS). Because the instrument is not sensitive to oxygen, data presented in this paper do not include the oxygen content.

Prior to the ^{129}Xe NMR experiments, samples were heated and outgassed under vacuum ($<10^{-4}$ Torr) for at least 4 h at 673 (± 5) K. The adsorption isotherms of natural xenon (99.99% pure, containing 26% xenon-129) were measured on a volumetric apparatus at xenon pressures between 3 and 1000 Torr. Xenon was adsorbed onto the samples at 300 K, the temperature at which the NMR spectra were recorded on a Bruker MSL 400 NMR spectrometer operating at 110.638 MHz. The conventional single-pulse Fourier transform technique was used with a radiofrequency pulse of 10 μs and a pulse delay of 1 s. The ^{129}Xe NMR chemical shifts are referenced to that of ^{129}Xe gas extrapolated to zero pressure. A KY zeolite reference sample (UOP) with a known chemical shift was used for calibration ($\delta = 134.8$ ppm from that of xenon gas at zero pressure). The uncertainty in the reported shifts is estimated to be ± 0.5 ppm. No paramagnetic impurities were detected by EPR on either sample.

RESULTS AND DISCUSSION

Catalytic Test

Epoxidation reactions catalyzed by titanium in silica-based catalysts and by TS-1 have been already described (23, 41–45). Differences between hex-1-ene and cyclohexene suggest that the reaction takes place inside the TS-1 pore system (46, 47). As we wished to differentiate the surface properties of the samples, epoxidation of a demanding substrate such as oct-1-ene with hydrogen peroxide seemed particularly appropriate. It should be emphasized that selective sorption by molecular sieves can give rise to unexpected selectivity effects (37). Another somewhat restricting factor influences the course of the reaction and the final product composition. Our previous work has shown that inorganic stabilizers, such as *phosphates*, incorporated into some commercial aqueous hydrogen peroxide solutions reduce the selectivity (1). It has also been found that under certain conditions the use of alkali metal *pyrophosphates* may deactivate or poison crystalline titanium-containing molecular sieves (48). The above considerations led us to use phosphate-free 30% aqueous H_2O_2 solutions (1) (see Experimental).

TABLE 1

Epoxidation of Oct-1-ene Catalyzed by TS-1 (A) and a Related Material (B) Using H_2O_2

Catalyst	Oct-1-ene conversion (%)	Epoxide selectivity (%)[a]
A	23	93
B	2	70

Note. Reaction conditions: catalyst wt., 0.050 g; acetone, 4.5 ml; oct-1-ene, 10.2 mmol; H_2O_2, 3.4 mmol (30% aqueous solution without phosphates); $T = 60°C$; reaction time, 2 h.

[a] See experimental; based on oct-1-ene, i.e., 100 (mol epoxide/mol oct-1-ene reacted).

The results for the two samples are presented in Table 1. Overall conversions and selectivities with samples A and B are significantly different. The final products obtained in oct-1-ene oxidation with these titanium catalysts compare well with those reported previously (1, 23, 39, 49). With catalyst A good epoxide selectivity is achieved; little of the hydrogen peroxide is wasted through dismutation to water and dioxygen. Sample B is markedly less selective and active than sample A. Ring opening reactions of the 1,2-epoxyoctane with water and/or acetone lead to the formation of 1,2-octanediol and 2,2-dimethyl-4-hexyl-3-dioxolane (see also Ref. 49) There is evidence for H_2O_2 dismutation. Additional characterization techniques were used to distinguish between active and less active catalysts. The samples were first characterized by the standard physicochemical methods; complementary information was obtained from ^{129}Xe NMR spectroscopy and electron microscopy with X-ray energy dispersion spectrometry.

Powder X-Ray Diffraction Data

The XRD patterns of the two samples are those of highly crystalline titanium silicalite (39) with a MFI structure (Fig. 1); they are indexed by analogy with the isotypic

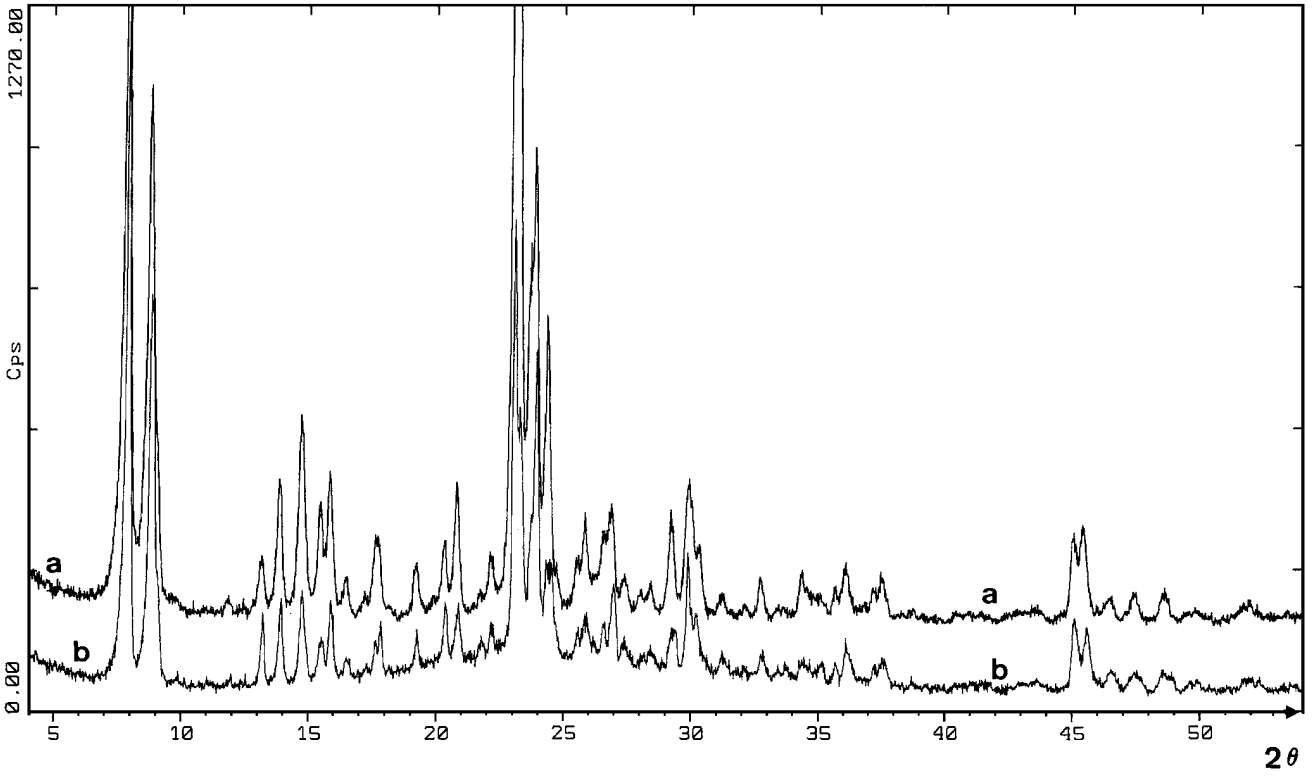

FIG. 1. X-ray powder diffraction patterns of samples A (a) and B (b) calcined at 555°C.

framework structures of silicalite-1 and zeolite ZSM-5 (50, 51). There are slight intensity differences; therefore, the unit cell parameters calculated by least-squares refinement of the patterns of samples A and B are very similar to the EUROTS-1 values (Table 2). They compare well with those of pure silicalite (50, 51), of TS-1 (39), and of ZSM-5 (50, 52).

As in the literature data (37, 39), there is evidence for orthorhombic symmetry. Because of the low titanium content in these materials, additional crystalline phases, if any, cannot be identified from the XRD patterns.

IR and Raman Spectra

A comparative IR spectrometric study was performed to obtain information concerning the existence of framework titanium. It is well known that the vibrational spectrum of TS-1 is characterized by an absorption band in the 900–975 cm^{-1} region (20, 21, 23, 39). This band is at 959 $\pm$ 4 cm^{-1} (medium intensity) for sample A and at 974 $\pm$ 4 cm^{-1} (weak) for B (Fig. 2). Its exact position depends on many parameters (amount of adsorbed water (18, 27), crystallite size (53), etc.). While the assignment is still questionable, this band may be considered the fingerprint of framework titanium. Among the various possible assignments are stretching mode (ν_3) of a [SiO_4] unit IR-active due to the presence of adjacent Ti (18), local stretching mode of a [TiO_4] and/or [O_3TiOH] unit in the silicalite framework (50), terminal Si–O stretching of SiOH···(HO)Ti "defective sites" (25), and a contribution of some or all of these species. Titanyl [Ti=O] vibrations might also contribute (17, 49). It has been suggested that the presence of a 960–975 cm^{-1} band is a necessary, but not sufficient, condition for catalytic activity (49). Thus, defective orthorhombic silicalites, with fully hydroxylated nanocavities generated by extraction of a few adjacent [SiO_4] units, have been characterized by an extra-broad IR absorption at *ca.* 960 cm^{-1} (25) and at 976 cm^{-1} in the Raman spectra (25). Therefore, framework titanium may be considered a structure defect rather than an atom isomorphously substituted for silicon in the silicalite lattice (54). The vibrational modes observed both in IR and in Raman spectra of TS-1 near 960 cm^{-1} were assigned to different components arising from the asymmetric

TABLE 2

Unit Cell Parameters[a] of MFI Molecular Sieves

Sample	*a* (Å)	*b* (Å)	*c* (Å)	Volume (Å^3)	Ref.
Silicalite-1	20.087 (2)	19.885 (4)	13.374 (2)	5341.9	(50, 51)
TS-1	20.133 (5)	19.933 (3)	13.416 (3)	5384.0	(39)
EUROTS-1	20.00 (4)	19.93 (4)	13.38 (5)	5333.3	(37)
A	20.047 (6)	19.865 (8)	13.403 (4)	5337.5	This work
B	20.106 (12)	19.922 (15)	13.428 (8)	5378.6	This work

[a] Standard deviations are given in parentheses.

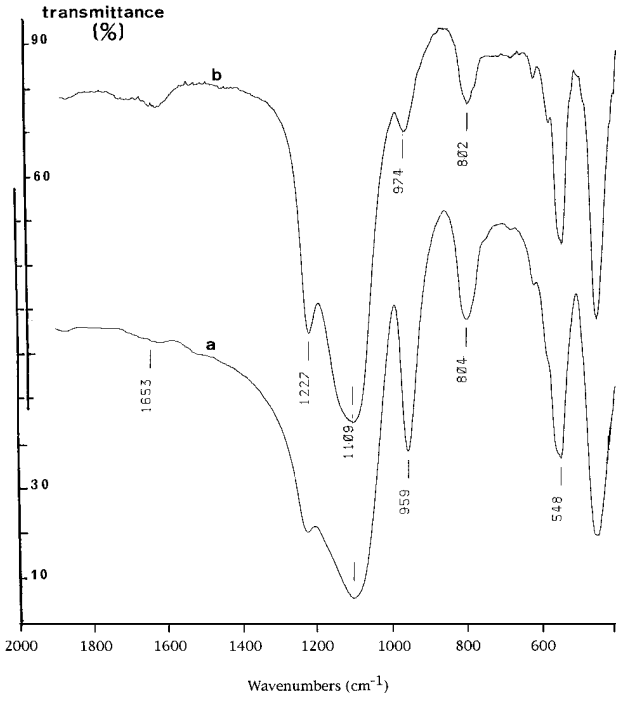

FIG. 2. IR spectra of samples A (a) and B (b) showing the change in intensity of the 959 and 974 cm^{-1} bands.

stretching modes of Si–O–Ti bridges (55). However, the observed band may be the resultant of several contributions.

In the light of previous work, as samples A and B have roughly the same particle size (*vide infra*) and nearly identical unit cell parameters (Table 2) and have been equilibrated to obtain nearly the same water content, we propose that the intensity differences in their spectra arise from dissimilarities in the titanium(IV) distribution. The peak at 959 cm^{-1} in sample A (Fig. 2) could correspond to a sample with a quasi-regular incorporation of titanium and that at 974 cm^{-1} (sample B) to an irregular distribution (*vide infra*). X-ray EDS, ^{129}Xe NMR, and Raman spectra (*vide infra*) give some support for this proposal. Raman and IR spectroscopy do not provide direct evidence regarding all the Ti–oxygen species, since some typical vibrations are in the same range as those of Si–oxygen moieties and the Si : Ti ratios are relatively high; however, with FT-Raman the samples can be analyzed without overwhelming background effects.

When extraframework titanium oxide species are present, they can belong to a segregated phase such as anatase TiO_2, which shows a strong Raman-active peak near 144 cm^{-1}. This peak could be detected on nearly amorphous TiO_2 materials obtained by sol–gel chemistry. Other weaker anatase Raman peaks occur at 386, 513, and 637 cm^{-1} (51). The conventional Raman spectra of sample A recorded on a Jobin–Yvon spectrometer indicate that anatase TiO_2 cannot be detected (spectra not shown). On the other hand, there is a broad signal near 144 cm^{-1} (Fig. 3 sample A) in the Fourier transform Raman spectra, which appears also in the spectra of pure silicalite, but no 640 cm^{-1} peak.

For sample B the anatase peak is observed as a sharp maximum at 144 cm^{-1}; moreover, Fig. 3 shows maxima near 510 (very weak) and 640 cm^{-1} which cannot be attributed to the silicalite framework and which have no counterpart in sample A or in the spectra of pure silicalite. A weak band appearing also at 961 cm^{-1} for sample B is very much stronger in sample A (964 cm^{-1}); hence, the peak at 144 cm^{-1} may be considered the fingerprint of anatase, the entire spectrum of B then being characteristic of a less ordered material if we consider the somewhat lower resolution of the spectrum (Fig. 3b). We can tentatively conclude from these results that in sample A the titanium is mainly or totally in the framework (nearly pure Ti-silicalite sample), while sample B contains both framework and

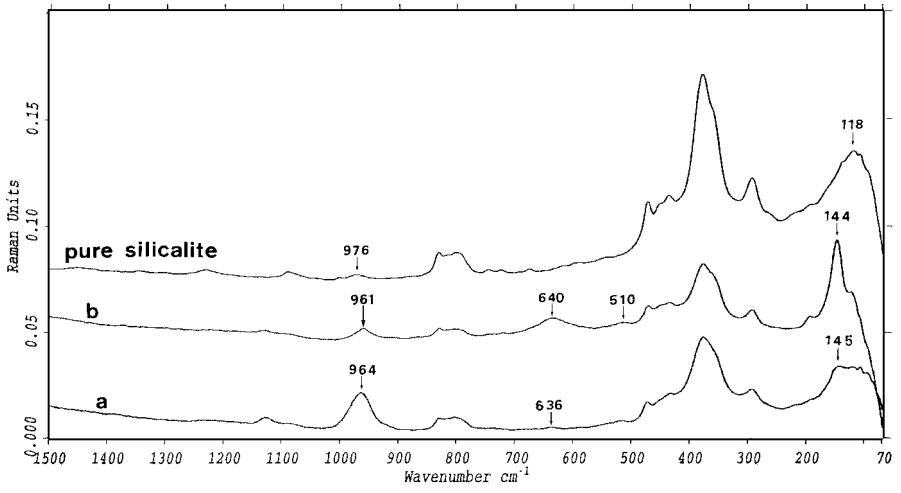

FIG. 3. Ambient temperature Fourier transform Raman spectra of samples A (a), B (b), and pure silicalite.

extraframework titanium (partly or totally in the form of anatase, which is not detected on the X-ray diffraction patterns). Small amounts of anatase (≈0.5 wt%) can be seen by Raman spectroscopy, and other forms of titanium oxide at very low concentration (less than 0.5 wt%) are weakly Raman diffusing (20). In addition to vibrational spectroscopy, UV–visible diffuse reflectance spectrometry was used to detect extraframework titanium.

Diffuse Reflectance Spectroscopy

For oxo species of Ti(IV), strong absorptions due to charge transfer (CT) transitions between O^{2-} and the central Ti(IV) atoms are expected in the UV–visible region. In the silicalite matrix, framework Ti(IV) is associated with absorptions at 210 nm in a tetrahedral environment and near 240 nm in an octahedral environment (20). For bulk TiO_2, the absorption threshold (interband transition) is observed near 410 nm (rutile) or 370 nm (anatase); in addition, when the particle size is lower than *ca.* 6–8 nm the band gap width increases and the threshold is shifted toward higher energies (shorter wavelengths).

Figure 4 shows clearly the existence of (i) intraframework isolated tetrahedral Ti(IV) ions in both samples, and (ii) extraframework bulk anatase in sample B (absorption threshold at 370 nm). On the other hand, the spectrum of sample A contains a weak shoulder near 316 nm (appearing as a slight inflexion on the SKM curve (not shown)), the corresponding threshold value (350 nm) attesting the presence of very small quantities of nanosized anatase particles (below *ca.* 4 nm).

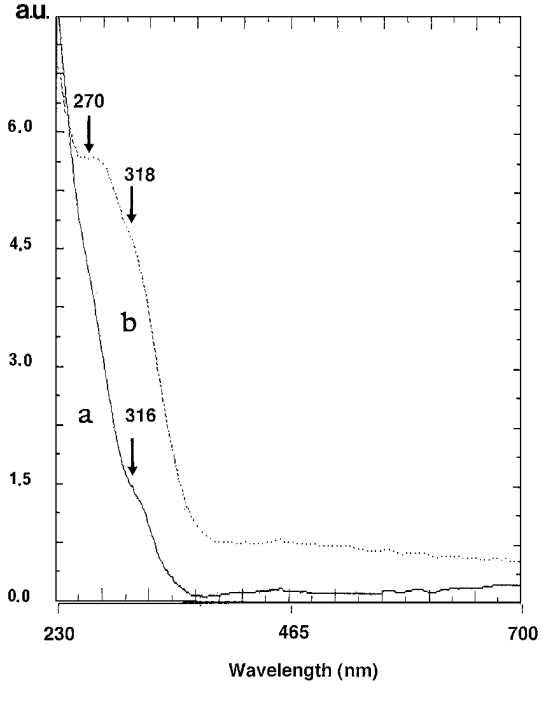

FIG. 4. UV–visible DRS spectra of samples A (a) and B (b).

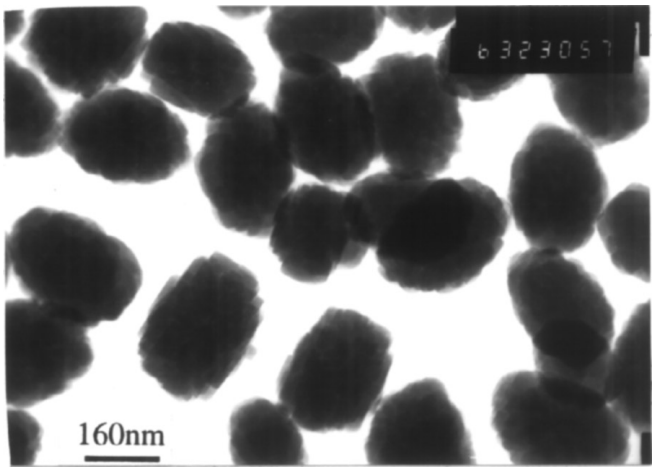

FIG. 5. TEM micrograph of sample A.

Electron Microscopy and X-Ray EDS

Transmission electron microscopy was used to obtain information about catalyst texture (mainly particle size and morphology). A representative TEM micrograph of sample A is shown in Fig. 5. The particles of sample A are highly crystalline with an average crystal size of 0.3 μm. This micrograph shows a very homogeneous product consisting of nonpolyhedral particles. As illustrated in Fig. 6, the majority of the particles of the sample B are orthorhombic while some are hexagonal prisms, all being about 0.3 μm in size. Nearly all the particles of samples A and B give diffraction patterns.

However, amorphous or poorly crystallized aggregates are also observed in sample B as very minor phase(s). In oxidations catalyzed by TS-1, the best yields were obtained with 0.2- to 0.3-μm crystallites; larger dimensions led to lower reaction rates and selectivities (38). In our case, the average particle sizes of samples A and B are quite similar.

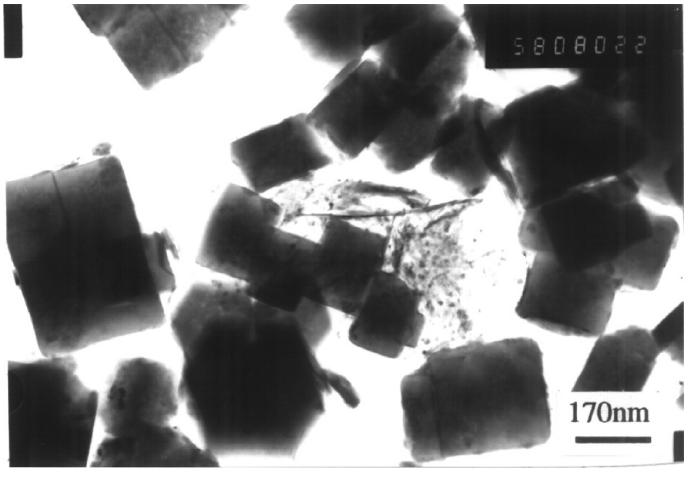

FIG. 6. TEM micrograph of sample B.

Morphology and particle size can influence the catalytic properties of the samples, but are not the key parameters explaining the observed catalytic differences (Table 1), as they appear to be in some cases (38).

Elemental analyses were performed on the two samples; the data (see Experimental and Tables 3–5) are to be compared with the X-ray EDS results.

Tables 3 to 5 list the results of X-ray EDS experiments used to locate and quantify submicroscopic distributions of the titanium species. EDS multiple spot analysis revealed that the titanium distribution in the sample A crystallites was homogeneous (Table 3), with at.% Ti ≈ 3.25 and a difference of 1.3% between maximum and minimum values. A typical analysis of ultramicrotomed sections of crystallites of sample A (Table 4) gives a mean at.% Ti of 2.6. Values for the core of the crystallites (grains 1–3) are lower (2.0–2.5%) than values for edges (2.5–3.4%). Sample B (Table 5), however, has a very inhomogeneous crystallite distribution; the majority of orthorhombic crystallites show an at.% Ti of 3.5, but typical differences between maximum and minimum values are 2.8%. Hexagonal crystals have a higher Ti content (≈4.45%) while amorphous aggregates have a very high titanium content and probably correspond to titanium oxides which cannot function effectively as catalytic sites in the H_2O_2 oxidations of olefins to epoxides (TiO_2 also evidenced by Raman and DRS examination). These results give further support for an atomic dispersion or a "homogeneous distribution" of the Ti sites in sample A, while in sample B there is a less ordered distribution between two (or more) phases and inside the different crystallites (orthorhombic and hexagonal-like). They are in agreement with the vibrational results and proposals. Even for samples A, we showed that titanium is not perfectly statistically distributed in the MFI structure: local analyses of atom ratios (Ti : Si) are considered to be the results of concentration gradients (compare Tables 3 and 4). We shall now try to differentiate these samples by ^{129}Xe NMR.

TABLE 3

X-Ray EDS on Catalyst A:[a] STEM Beam Analyses on Various Zones of Different Crystallites and Comparison with Analyses of Relatively Large Domains and with Bulk Chemical Composition

Type	Zone (nm^2)	At.% Si	At.% Ti	Si/Ti
Grain 1	150 × 200	96.5	3.5	27.6
Grain 2	200 × 270	96.4	3.6	26.8
Grain 3	150 × 200	96.8	3.2	30.25
Grain 4	150 × 200	96.5	3.5	27.6
	1260[b]	97.1	2.9	33.5
	1260[b]	96.7	3.3	29.3
Grain 5	1260[b]	96.9	3.1	31.25
	1260[b]	96.7	3.3	29.3
Grain 6	1260[b]	96.3	3.7	26.0
	1260[b]	97.6	2.4	40.7
Averaged composition		96.75	3.25	29.75
Chemical analysis		97.45	2.55	38.2

[a] Data do not include oxygen; counting time, 400 s.
[b] Diameter of the observed zone: 40 nm (spot beam analysis).

TABLE 4

X-Ray EDS on Catalyst A:[a] STEM Beam Analyses of Ultramicrotomed Crystallites (Edges and Cores) Compared with Larger Zone Analyses and with Bulk Chemical Composition

Type	Zone (nm^2)	At.% Si	At.% Ti	Si/Ti
Section	150 × 200	96.8	3.2	30.25
Section	120 × 160	97.7	2.3	42.5
Section	600 × 800	97.9	2.1	46.6
Section	600 × 800	97.3	2.7	36.0
Section	150 × 200	97.2	2.8	34.7
Core	1260[b]	96.75	3.25	29.75
Core	1260[b]	97.3	2.7	36.0
Core	1260[b]	97.6	2.4	40.7
Core, grain No. 1	180[c]	98.0	2.0	49
Edge, grain No. 1	180[c]	97.4	2.6	37.5
Core, grain No. 2	180[c]	97.5	2.5	39
Edge, grain No. 2	180[c]	96.6	3.4	28.4
Core, grain No. 3	180[c]	97.9	2.1	46.6
Edge, grain No. 3	180[c]	97.5	2.5	39
Small domain, grain No. 3	180[c]	97.8	2.2	44.45
Averaged composition		97.4	2.6	37.5
Chemical analysis		97.45	2.55	38.2

[a] Data do not include oxygen; counting time, 200–400 s.
[b, c] Diameters of the observed zone: [b] 40 and [c] 15 nm.

Study of Samples by ^{129}Xe NMR: Theoretical Aspects

^{129}Xe NMR of adsorbed xenon provides information about microporous molecular sieves difficult to obtain by classical physicochemical techniques. The dimensions of cages and/or channels (i.e. the pore free volume), the locations of compensating cations, pore blocking, and intergrowths or defects related to short-range crystallinity have

TABLE 5

X-Ray EDS on Catalyst B:[a] STEM Beam Analyses of Different Crystallites

Type	Zone (nm^2)	At.% Si	At.% Ti	Si/Ti
Hexagonal prisms	120 × 160	95.2	4.8	19.8
Hexagonal prisms	150 × 200	95.9	4.1	23.4
Amorphous grain[b]	100 × 130	83.5	16.5	5.1
Orthorhombic crystal	120 × 160	95.9	4.1	23.4
Orthorhombic crystal	150 × 200	95.3	4.7	20.3
Orthorhombic crystal	120 × 160	97.1	2.9	33.5
Orthorhombic crystal	200 × 270	97.6	2.4	40.7
Orthorhombic crystal	100 × 130	98.1	1.9	51.6
Averaged composition[b]		96.45	3.5	27.2
Chemical analysis		96.95	3.05	31.8

[a] Data do not include oxygen; counting time, 100–200 s.
[b] Minor phase, excluded from the averaged composition.

an effect on the chemical shift of adsorbed xenon (55–57). The variation of the measured chemical shift, δ_{exp}, with the number of adsorbed xenon atoms per gram of anhydrous sample, n, depends on the molecular sieve structure. The chemical shift of ^{129}Xe has been written as the sum of terms corresponding to the different perturbations to which the system is submitted. For xenon adsorbed in a pure (diamagnetic) sample of silicalite, δ_{exp} is expressed as

$$\delta_{exp} \approx \delta_0 + \delta_S + \delta_{Xe}, \quad [1]$$

where δ_0 is the reference (usually the chemical shift of gaseous xenon extrapolated to zero pressure) and δ_S corresponds to interactions between Xe and cage or channel walls. This term has been related to the pore or channel size (void space) via the mean free path, defined as the average distance between two successive collisions of a single Xe atom with the internal surface (55). The last term, δ_{Xe}, corresponds to the increase in shift caused by Xe–Xe collisions. It increases with n and is responsible for the slope of the $\delta_{exp} = f(n)$ curves.

If there are adsorption sites stronger than the pore wall, such as multivalent cations, metallic particles, or nonframework species, Eq. [1] includes additional terms corresponding to these specific interactions.

Xenon Adsorption Isotherms

The 300 K isotherms expressed in logarithmic coordinates are of the classical form for xenon adsorption in molecular sieves (Fig. 7): $\log n$ increases linearly with $\log P_{Xe}$ at low values of the xenon pressure, P_{Xe}. The uptake tends toward saturation values at high pressure.

At 1000 Torr, pure silicalite and sample A adsorb nearly the same amount of xenon, 1.2×10^{21} and 1.3×10^{21} Xe atoms g^{-1}, respectively. For sample B, the amount adsorbed (0.6×10^{21} Xe atoms g^{-1}) is significantly lower and very near the saturation value (Fig. 7). Since the results of X-ray diffraction show that the crystallinities are comparable, the decrease of the adsorption capacity of sample B must be due to pore blocking by some extraframework species.

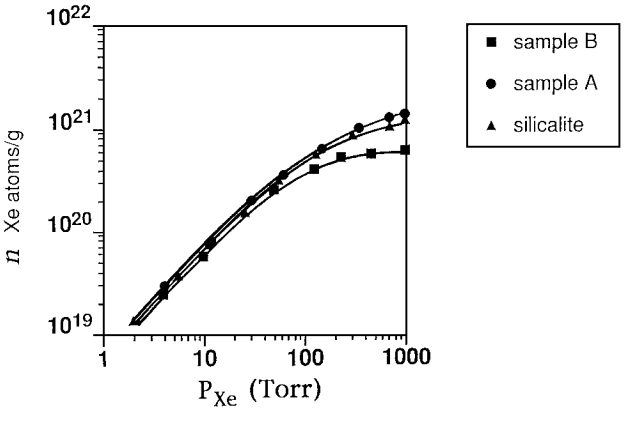

FIG. 7. Uptake of xenon by sample A (●), pure silicalite (▲), and sample B (■) at 300 K.

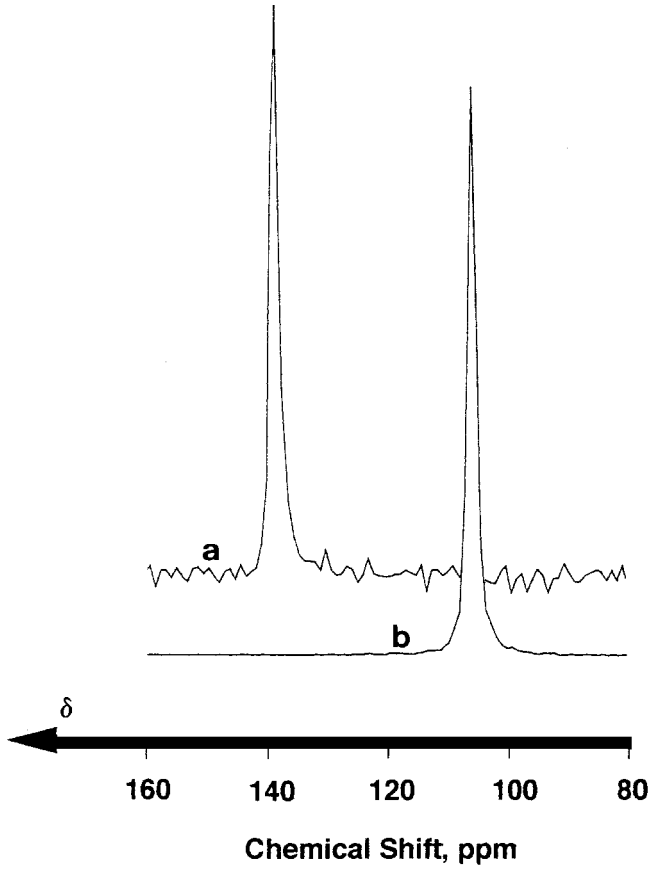

FIG. 8. NMR spectra of xenon-129 adsorbed on samples A (a) ($n \approx 11 \times 10^{20}$ Xe atoms/g) and B (b) ($n \approx 2 \times 10^{20}$ Xe atoms/g) at 300 K.

^{129}Xe NMR Study of Adsorbed Xenon in Samples A and B

The ^{129}Xe NMR spectra of the three silicalite-based samples consist of a single narrow peak when n is in the range 1.0×10^{20}–1.2×10^{21} (Fig. 8). This result suggests that there are no obvious structural defects, such as larger pore volumes.

The dependence of the chemical shift on n presents the same trends: the variations are rather linear with a change of slope at a certain n value (Fig. 9). The plots are very similar for sample A and pure silicalite. The change of slope occurs at a characteristic value, n_c (5.5×10^{20} Xe atoms g^{-1}), and the δ_S values (103 ppm) obtained by extrapolation of the $\delta_{exp} = f(n)$ curves to $n = 0$ are equal. For sample B, however, the slopes are greater and the change of slope occurs at about $n_c = 3.7 \times 10^{20}$ Xe atoms g^{-1}; the value of δ_S is 100 ppm.

Such typical curves have already been observed for ZSM-5 (and ZSM-11) zeolites (56) which have very similar

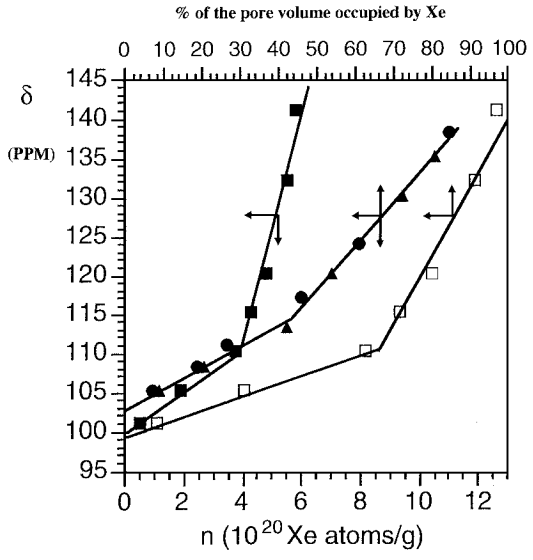

FIG. 9. Xenon-129 chemical shift, δ_{exp}, as a function of n in pure silicalite (▲) and samples A (●) and B (■) at 300 K, as a function of the percentage of the pore volume occupied by xenon in samples B and A or silicalite as reference samples.

structures (50). A possible explanation of the change in slope is a change in the Xe–Xe interactions at a certain n (56). Because of their dimensions the channels must be a little more efficient than the intersections for adsorbing xenon. Therefore, at low concentration, the xenon atoms spend a longer time in the channels, where only one xenon atom can be adsorbed between two intersections. The probability of Xe–Xe collisions is low and xenon atoms interact little with each other; consequently the slope of the $\delta_{exp} = f(n)$ curves is small. At a certain xenon concentration, Xe atoms begin significantly to occupy the intersections, where they can interact with Xe in the channels. In this case Xe–Xe interactions become important, three-body collisions are no longer negligible, and the slope is much higher (second part of the plots).

Let us consider first the δ_S values. δ_S depends on the mean free path of xenon and is directly related to the dimensions of the internal voids but also to the ease of diffusion inside the channels (55). The greater the pores, the smaller the δ_S values. The same value (103 ppm) obtained for sample A and the reference sample (pure silicalite) proves that the pore structure of sample A has not been modified by the incorporation of Ti into the framework. On the other hand, δ_S for sample B is a little smaller, which means that the mean free path of Xe is greater. This may be related to the presence of a small number of randomly distributed structural defects, hardly larger than that of normal channels, δ_S being an average value due to rapid exchange of xenon between normal channels and defects.

Let us now analyze the slope, S, of the second linear part ($n > n_c$) of the $\delta_{exp} = f(n)$ curves for samples A and B (Fig. 9). The values of this slope are

$$S_{(A)} = 4.5 \times 10^{-20} \text{ ppm atoms}^{-1}\ g^{+1}$$
$$S_{(B)} = 8.7 \times 10^{-20} \text{ ppm atoms}^{-1}\ g^{+1}.$$

δ_{Xe} is due to Xe–Xe interactions and depends on the local xenon density. Therefore, for a given structure, S is inversely proportional to the total free volume, which is itself proportional to the quantity of adsorbed xenon at saturation. In the present case, while the amounts of xenon adsorbed near saturation, n_{sat}, are similar for the reference silicalite and sample A (*ca.* $1.2–1.3 \times 10^{21}$ Xe atoms g^{-1}), sample B adsorbs much less at saturation, 0.6×10^{21} Xe atoms g^{-1} (Fig. 7). On the other hand, Fig. 9 shows that the slope for sample B is much greater than that for sample A for $n > n_c$. However, their ratio, $S_{(B)}/S_{(A)} = 1.9$, is roughly equal to the ratio $n_{sat(A)}/n_{sat(B)}$ (*ca.* 2). We can conclude that sample B does not contain amorphous material able to adsorb xenon. The decrease in adsorption capacity may be due rather to pore blocking of the silicalite.

Can we locate this pore blocking? The change of the slope occurs, for sample B, at a much higher value of the xenon concentration, expressed as the percentage of the pore volume occupied by xenon (see Fig. 9, upper abscissa scale). Since the first part of the $\delta_{exp} = f(n)$ curves corresponds to xenon adsorbed mainly in the channels (rather than in the intersections), this may be attributed to a decrease in the total free volume of sample B, whose origin is principally a decrease in the volume of the intersections. In other words, the extraframework species blocking the pores might be located in some of the intersections rather than in the channels.

CONCLUSION

The unique catalytic properties of titanium silicalites are certainly due to the Ti(IV) coordination facilitating reactions, or to the "atomic dispersion" of titanium, or both. The determination of the %Ti/(%Ti + %Si) ratios by X-ray EDS and ^{129}Xe NMR studies of two samples of "titanium silicalite" show that these are promising methods for characterizing diamagnetic transition metal-containing molecular sieves, TMCMS, and in particular for identifying the synthesized materials with respect to the location and the nature of the Ti-species within the MFI structure. The NMR spectrum of xenon adsorbed in TS-1 and related materials with the MFI structure is sensitive to impurities, such as small amounts of extraframework titania (crystalline anatase or amorphous phase), and *to pore blocking.* The dependence of δ_{exp} on n indicates that xenon–xenon interactions are modified by impurities, by imperfect distribution of the Ti sites, and by occluded titania; on the other hand, pure silicalite and nearly perfect TS-1 cannot be differentiated by ^{129}Xe NMR, since the channel dimensions along [010] and [100] (straight

and sinusoidal channels, respectively) are nearly the same and so probably are the potentials along the channels. FT-Raman and IR spectra are tentatively interpreted in terms of differences in the "atomic dispersion" of Ti(IV), since the crystallization states of the two samples are not differentiated by the X-ray diffraction patterns though they are easily identified by FT-Raman spectra. The spectral differences between the catalysts are correlated with their different catalytic reactivities; the change of conversion and selectivity in the epoxidation of oct-1-ene can be related to the quality (phosphate-free or not) of H_2O_2 (1) but also to the acidity of TS-1, which must be related to the statistical distribution of titanium in the framework, to the presence of extraframework titanium, and to pore blocking. The present work confirms the ability of UV–visible DRS to distinguish between intra- and extraframework titanium species. These methods can also be used to characterize other transition metal-containing materials, such as "redox molecular sieves" and novel tailor-made catalysts based on mesoporous solids, which are being studied in our groups.

ACKNOWLEDGMENTS

We thank ADEME for a grant to E.D. and Dr. J. S. Lomas for constructive discussions and for correcting the manuscript. We also thank Enichem and Rhône-Poulenc for providing some TS-1 samples, Drs. G. Chottard, C. Lehner, and J. C. Boulou for the Raman spectra, and M. Lavergne for preparing the microtomed samples. This paper is dedicated to Dr. C. Jeanmart.

REFERENCES

1. Duprey, E., Maquet, J., Man, P. P., Manoli, J.-M., Delamar, M., and Brégeault, J.-M., *Appl. Catal. A* **128**, 89 (1995).
2. Salles, L., Aubry, C., Thouvenot, R., Robert, F., Dorémieux-Morin, C., Chottard, G., Ledon, H., Jeannin, Y., and Brégeault, J.-M., *Inorg. Chem.* **33**, 871 (1994).
3. Brégeault, J.-M., Thouvenot, R., Zoughebi, S., Salles, L., Atlamsani, A., Duprey, E., Aubry, C., Robert, F., and Chottard, G., *Stud. Surf. Sci. Catal.* **82**, 571 (1994).
4. Bellussi, G., and Rigutto, M. S., *Stud. Surf. Sci. Catal.* **85**, 177 (1995) and references therein.
5. Ratnasamy, P., and Kumar, R., *Catal. Lett.* **22**, 227 (1993).
6. Notari, B., *Catal. Today* **18**, 163 (1993).
7. Sheldon, R. A., and Dakka, J., *Catal. Today* **19**, 215 (1994).
8. Dartt, C. B., and Davis, M. E., *Ind. Eng. Chem. Res.* **33**, 2887 (1994).
9. Schirmann, J.-P., and Delavarenne, S. Y., "Hydrogen Peroxide in Organic Chemistry," Edition et Documentation Industrielle, Paris, 1979, and references therein.
10. Strukul, G. (Ed.), "Catalytic Oxidations with Hydrogen Peroxide as Oxidant," Kluwer Academic, Dordrecht, 1992, and references therein.
11. Starks, C. M., Liota, C. L., and Halpern, M., "Phase-Transfer Catalysis, Fundamentals, Applications and Industrial Perspectives," pp. 500–564, Chapman & Hall, New York, 1994; Dehmlov, E. V., and Dehmlov, S. S., "Phase Transfer Catalysis," pp. 344–349, VCH, Weinhein, 1993.
12. Notari, B., *Stud. Surf. Sci. Catal.* **67**, 243 (1991).
13. Varagnat, J., *Ind. Eng. Chem. Prod. Res. Dev.* **15**, 212 (1976).
14. Costantini, M., Manaut, D., and Michelet, D., European Patents 606182A1 and 606183A1, 1994 (to Rhône-Poulenc Chimie).
15. Roffia, P., Leofanti, G., Cesana, A., Mantegazza, M., Padovan, M., Petrini, G., Tonti, S., and Gervasutti, P., *Stud. Surf. Sci. Catal.* **55**, 43 (1990).
16. Thangaraj, A., Sivasanker, S., and Ratnasamy, P., *J. Catal.* **131**, 394 (!991).
17. Perego, G., Bellussi, G., Corno, C., Taramasso, M., Buonomo, F., and Esposito, A., *Stud. Surf. Sci. Catal.* **28**, 129 (1986).
18. Boccuti, M. R., Rao, K. M., Zecchina, A., Leofanti, G., and Petrini, G., *Stud. Surf. Sci. Catal.* **48**, 133 (1989).
19. Tuel, A., Diab, J., Gelin, P., Dufaux, M., Dutel, J.-F., and Ben Taarit, Y., *J. Mol. Catal.* **63**, 95 (1990).
20. Zecchina, A., Spoto, G., Bordiga, S., Ferrero, A., Petrini, G., Leofanti, G., and Padovan, M., *Stud. Surf. Sci. Catal.* **69**, 251 (1991).
21. Zecchina, A., Spoto, G., Bordiga, S., Padovan, M., Leofanti, G., and Petrini, G., *Stud. Surf. Sci. Catal.* **65**, 671 (1991).
22. Millini, R., Previde Massara, E., Perego, G., and Bellussi, G., *J. Catal.* **137**, 497 (1992).
23. Huybrechts, D. R. C., Buskens, P. L., and Jacobs, P. A., *J. Mol. Catal.* **71**, 129 (1992).
24. Tuel, A., and Ben Taarit, Y., *J. Chem. Soc. Chem. Comm.*, 1578 (1992).
25. Scarano, D., Zecchina, A., Bordiga, S., Geobaldo, F., Spoto, G., Petrini, G., Leofanti, G., Padovan, M., and Tozzola, G., *J. Chem. Soc. Faraday Trans.* **89**, 4123 (1993).
26. de Castro-Martins, S., Tuel, A., and Ben Taarit, Y., *Zeolites* **14**, 130 (1994).
27. Lopez, A., Tuilier, M. H., Guth, J. L., Delmotte, L., and Popa, J. M., *J. Solid State Chem.* **102**, 480 (1993).
28. Behrens, P., Felsche, J., Vetter, S., Schulz-Ekloff, G., Jaeger, N. I., and Niemann, W., *J. Chem. Soc. Chem. Commun.*, 678 (1991).
29. Schultz, E., Ferrini, C., and Prins, R., *Catal. Lett.* **14**, 221 (1992).
30. Bonneviot, L., Trong On, D., and Lopez, A., *J. Chem. Soc. Chem. Commun.*, 685 (1993).
31. Pei, S., Zajac, G. W., Kaduk, J. A., Faber, J., Boyanov, B. I., Duck, D., Fazzini, D., Morrison, T. I., and Yang, D. S., *Catal. Lett.* **21**, 333 (1993).
32. Bordiga, S., Boscherini, F., Coluccia, S., Genoni, F., Lamberti, C., Leofanti, G., Marchese, L., Petrini, G., Vlaic, G., and Zecchina, A., *Catal. Lett.* **26**, 195 (1994).
33. Crocco, G. L., and Zajacek, J. G., European Patent 0568336A2, 1993 (to Arco).
34. Thangaraj, A., Kumar, R., Mirajkar, S. P., and Ratnasamy, P., *J. Catal.* **130**, 1 (1991).
35. Reddy, J. S., Kumar, R., and Ratnasamy, P., *Appl. Catal.* **58**, L1 (1990).
36. Popa, J. M., Guth, J. L., and Kessler, H., European Patent Application No. 292 363, 1988 (to Rhône-Poulenc Chimie).
37. Martens, J. A., Buskens, P., Jacobs, P. A., van der Pol, A. J. H. P., van Hooff, J. H. C., Ferrini, C., Kouwenhoven, H. W., Kooyman, P. J., and van Bekkum, H., *Appl. Catal. A* **99**, 71 (1993).
38. van der Pol, A. J. H. P., Verduyn, A. J., and van Hooff, J. H. C., *Appl. Catal. A* **92**, 113 (1992).
39. Taramasso, M., Perego, G., and Notari, B., U.S. Patent 4,410,501, 1983 (to Snamprogetti S.p.A).
40. Leglise, J., Manoli, J.-M., Potvin, C., Djega-Mariadassou, G., and Cornet, D., *J. Catal.* **152**, 275 (1995).
41. Neri, C., Anfossi, B., Esposito, A., and Buonomo, F., European Patent 0100119 A1, 1983 (to Eni).
42. Maspero, F., and Romano, U., European Patent 0190609A2, 1986 (to Eni).
43. Clerici, M. G., and Romano, U., European Patent 0230949A2, 1987 (to Eni).
44. Clerici, M. G., and Bellusi, G., European Patent 0315247A1, 1988 (to Eni).
45. Clerici, M. G., and Bellusi, G., European Patent 0315248A1, 1988 (to Eni).

46. Clerici, M. G., and Ingallina, P., *J. Catal.* **140**, 71 (1993).
47. Tatsumi, T., Nakamura, M., Yuasa, K., and Tominaga, H., *Chem. Lett.*, 297 (1990).
48. Saxton, R. J., Zajacek, J. G., and Crocco, G. L., U.S. Patent 5,374,747, 1994 (to Arco).
49. Huybrechts, D. R. C., Vaesen, I., Li, H. X., and Jacobs, P. A., *Catal. Lett.* **8**, 237 (1991).
50. Meier, W. M., and Olson, D. H., "Atlas of Zeolite Structure Types," 3rd rev. ed. pp. 138–139, 192–193, Butterworths–Heinemann, London, 1992.
51. Dartt, C. B., Khouw, C. B., Li, H. X., and Davis, M. S., *Microporous Mater.* **2**, 425 (1994); Pilz, W., Penker, Ch., Tuan, V. A., Fricke, R., and Kosslick, H., *Ber. Bunsenges. Phys. Chem.* **97**, 1037 (1993).
52. Wu, E. L., Lawton, S. L., Olson, D. H., Rohrman, A. C., and Kokotailo, G. T., *J. Phys. Chem.* **83**, 2777 (1979).
53. Bellussi, G., Carati, A., Clerici, M. G., Maddinelli, G., and Millini, R., *J. Catal.* **133**, 220 (1992).
54. Jacobs, P. A., *in* "Selective Oxidations in Petrochemistry," DGMK Conference, Goslar, Sept. 16–18, 1992, p. 171.
55. Astorino, E., Peri, J. B., Willey, R. J., and Busca, G., *J. Catal.* **157**, 482 (1995).
56. Springuel-Huet, M. A., Bonardet, J.-L., and Fraissard, J., *Appl. Magn. Reson.* **8**, 427 (1995) and references therein.
57. Chen, Q., Springuel-Huet, M. A., Fraissard, J., Smith, M. L., Corbin, D. R., and Dybowski, C., *J. Phys. Chem.* **96**, 10,914 (1992).
58. Ito, T., and Fraissard, J., *J. Chem. Phys.* **76**, 5225 (1982).